

Recovering galaxy cluster gas density profiles with *XMM-Newton* and *Chandra*

I. Bartalucci^{1,2}, M. Arnaud^{1,2}, G. W. Pratt^{1,2}, A. Vikhlinin³, E. Pointecouteau⁴, W. R. Forman³, C. Jones³,
P. Mazzotta^{3,5}, and F. Andrade-Santos³

¹ IRFU, CEA, Université Paris-Saclay, 91191 Gif-Sur-Yvette, France
e-mail: iacopo.bartalucci@cea.fr

² Université Paris Diderot, AIM, Sorbonne Paris Cité, CEA, CNRS, 91191 Gif-sur-Yvette, France

³ Harvard-Smithsonian Center for Astrophysics, 60 Garden Street, Cambridge, MA 02138, USA

⁴ IRAP, Université de Toulouse, CNRS, UPS, CNES, 31042 Toulouse, France

⁵ Dipartimento di Fisica, Università di Roma Tor Vergata, via della Ricerca Scientifica 1, 00133 Roma, Italy

Received 1 August 2017 / Accepted 14 September 2017

ABSTRACT

We examined the reconstruction of galaxy cluster radial density profiles obtained from *Chandra* and *XMM-Newton* X-ray observations, using high quality data for a sample of twelve objects covering a range of morphologies and redshifts. By comparing the results obtained from the two observatories and by varying key aspects of the analysis procedure, we examined the impact of instrumental effects and of differences in the methodology used in the recovery of the density profiles. We find that the final density profile shape is particularly robust. We adapted the photon weighting vignetting correction method developed for *XMM-Newton* for use with *Chandra* data, and confirm that the resulting *Chandra* profiles are consistent with those corrected a posteriori for vignetting effects. Profiles obtained from direct deprojection and those derived using parametric models are consistent at the 1% level. At radii larger than $\sim 6''$, the agreement between *Chandra* and *XMM-Newton* is better than 1%, confirming an excellent understanding of the *XMM-Newton* PSF. Furthermore, we find no significant energy dependence. The impact of the well-known offset between *Chandra* and *XMM-Newton* gas temperature determinations on the density profiles is found to be negligible. However, we find an overall normalisation offset in density profiles of the order of $\sim 2.5\%$, which is linked to absolute flux cross-calibration issues. As a final result, the weighted ratios of *Chandra* to *XMM-Newton* gas masses computed at R_{2500} and R_{500} are $r = 1.03 \pm 0.01$ and $r = 1.03 \pm 0.03$, respectively. Our study confirms that the radial density profiles are robustly recovered, and that any differences between *Chandra* and *XMM-Newton* can be constrained to the $\sim 2.5\%$ level, regardless of the exact data analysis details. These encouraging results open the way for the true combination of X-ray observations of galaxy clusters, fully leveraging the high resolution of *Chandra* and the high throughput of *XMM-Newton*.

Key words. methods: data analysis – galaxies: clusters: intracluster medium – X-rays: galaxies: clusters

1. Introduction

Clusters of galaxies provide valuable information on cosmology, from the physics driving galaxy and structure formation to the nature of dark energy (see e.g. Voit 2005; Allen et al. 2011). Clusters are primarily composed of dark matter, the baryonic component being contained mainly in the form of hot ionised plasma that fills the intra-cluster volume, namely the intra-cluster medium (ICM). The ICM emits in the X-ray band primarily via thermal Bremsstrahlung, which depends on the plasma density and temperature.

X-ray observations play a key role in studying the ICM emission. In particular, the advent of high resolution spectro-imaging observations from *Chandra* and *XMM-Newton* has yielded a rich ensemble of observations to be studied and understood. In the context of galaxy cluster observations these two satellites are complementary: the unprecedented angular resolution of *Chandra* is well-suited to exploring the bright central parts, while the large effective area of *XMM-Newton* allows detection of the emission up to large radial distances, where the X-ray signal becomes very faint. A combination of these instruments can in principle be used to obtain more precise (especially in the centre) and spatially extended profiles

(e.g. Bartalucci et al. 2017). However, previous works combining datasets from the two satellites have found systematic differences due to cross-calibration issues (e.g. Snowden et al. 2008; Mahdavi et al. 2013; Martino et al. 2014; Schellenberger et al. 2015). For the hottest clusters, *Chandra* temperatures are found to be higher than those of *XMM-Newton* by 10–15% while the flux offset is smaller, at ~ 1 –3%, and consistent with zero. Furthermore, as instruments are routinely monitored throughout the spacecraft lifetime and as in-flight calibration is undertaken, these systematic differences can evolve considerably depending on the version of the calibration database, CALDB, used for each satellite.

Here we focus uniquely on the reconstruction of gas density profiles and the calculation of integrated gas masses from *XMM-Newton* and *Chandra* data. The gas density should, in principle, be trivial to recover since the observed X-ray surface brightness is proportional to the line-of-sight integral of the square of the density, times the X-ray cooling function, which in turn is almost independent of temperature in the soft energy band. Thus the absolute temperature calibration will have a minimal effect on the recovered density (shown explicitly in Sect. 4.4). However, a number of other potential sources of

Table 1. Observational properties of the 12 clusters used in this work.

Cluster name	RA	Dec	z	N_{H}^a [10^{20} cm^{-3}]	<i>Chandra</i> exp. [ks]	<i>XMM-Newton</i> exp. (MOS1,2; PN) [ks]	<i>Chandra</i> obs. ID	<i>XMM-Newton</i> obs. ID
	[J2000]	[J2000]						
A1651	12 59 22.15	−04 11 48.24	0.084	1.81	10	7; 5	4185	0203020101
A1650	12 58 41.48	−01 45 40.45	0.084	0.72	37	34; 30	7242	0093200101
A1413	11 55 17.97	+23 24 21.99	0.143	1.84*	75	63; 52	5003	0502690201
A2204	16 32 46.94	+05 34 32.63	0.152	6.97*	77	14; 10	7940	0306490201
A2163	16 15 46.06	−06 08 52.36	0.203	16.50*	71	92; 65 [†]	1653	0694500101
A2390	21 53 36.82	+17 41 43.30	0.231	8.66	95	10; 8	4193*	0111270101
MACS J1423.8+2404	14 23 47.92	+24 04 42.96	0.545	2.20	115	34; 22 [†]	4195*	0720700301
MACS J0717.5+3745 ^b	07 17 31.75	+37 45 31.02	0.546	6.64	58	59; 52	16305	0672420201
MACS J0744.9+3927	07 44 52.78	+39 27 26.63	0.698	5.66	50	52; 42 [†]	6111	0551851201
SPT-CL J2146−4633	21 46 34.72	−46 32 50.86	0.933	1.64	80	90; 64 [†]	13469	0744400501
SPT-CL J2341−5119	23 41 12.23	−51 19 43.05	1.003	1.21	50	64; 34 [†]	11799	0744400401
SPT-CL J0546−5345	05 46 37.22	−53 45 34.43	1.066	6.77	27	45; 33 [†]	9336	0744400201

Notes. The coordinates indicate the position of the X-ray peak used as the centre for profile extraction. The peak was determined using *Chandra* observations in the [0.7–2.5] keV band. ^(a) The neutral hydrogen column density was derived from the LAB survey (Kalberla et al. 2005). ^(b) The X-ray peak is centred on the main structure, identified as region “B” in Limousin et al. (2016). ^(c) The absorption value was estimated in a region which maximises the S/N. ^(†) MOS 2 effective exposure times are 3–4% higher than MOS1, except for MACS J1423.8+2404, for which the MOS2 exposure time is 43 ks. ^(*) ACIS-S observations.

systematic difference still remain, including: the absolute flux calibration; the exclusion of substructure and point sources; for *XMM-Newton*, the correction for the point spread function (PSF); the method used to correct for the vignetting of the X-ray telescopes; or whether the analysis uses a parametric or a non-parametric approach. Here we have compared the ICM density profiles obtained using variations on two approaches developed for statistical studies of clusters – that of the *Chandra* Cluster Cosmology Project (CCCP; Vikhlinin et al. 2009a) for *Chandra*, and that of REXCESS (Croston et al. 2008; Pratt et al. 2009) for *XMM-Newton*. The Planck Collaboration have also used the latter method (e.g. Planck Collaboration XI 2011; Planck Collaboration Int. III 2013; Planck Collaboration XX 2014). Our choice is motivated by the fact that each approach is representative of a standard analysis for its respective satellite, while being sufficiently different in procedure (notably in the treatment of vignetting, or in the choice of parametric vs. non-parametric modelling of the X-ray surface brightness) to allow investigation of some of the issues mentioned above. We can also use the exceptional PSF of *Chandra* to test the robustness of the *XMM-Newton* PSF correction procedure, which is one of the main analysis issues when reconstructing the central regions of the gas density profiles. This is particularly true for evolution studies, because of the decrease of the angular size with the redshift. Hence we focus on a sample in a wide redshift range, up to $z \sim 1$.

The paper is organised as follows: in Sect. 2 we present the sample of the clusters used in this work, and in Sect. 3 we detail the various data analysis steps and methods used to reconstruct the radial density distribution from the surface brightness profiles. In Sect. 4, we describe the tests we use to assess and quantify the robustness of the density profile reconstruction, and detail the comparison between the two instruments. Our conclusions are presented in Sect. 6.

We adopted a cold dark matter cosmology with $\Omega_{\text{M}} = 0.3$, $\Omega_{\Lambda} = 0.7$ and $H_0 = 70 \text{ km Mpc}^{-1} \text{ s}^{-1}$ throughout. All errors are reported at the 1σ level. The quantity R_{500} is defined as the radius at which the total density of the cluster is 500 times the critical density.

2. Cluster sample

As this work is dedicated to a systematic comparison of the ICM properties derived from *Chandra* and *XMM-Newton* observations, we required (1) sufficient exposure time to allow extraction of well-sampled radial profiles at least up to $\sim R_{500}$; (2) a wide redshift range to test the effect of different angular sizes on the PSF reconstruction; (3) different X-ray morphologies to examine the effect of features such as, for example, peaked or flat central emission. Following these criteria we defined a sample of twelve clusters whose main observational properties are reported in Table 1. We limited our datasets to single observations to simplify the analysis and avoid complications related to the creation of mosaics.

All the clusters in our sample have been observed using the *Chandra* Advanced CCD Imaging Spectrometer (ACIS, Garmire et al. 2003) and the *XMM-Newton* European Photon Imaging Camera (EPIC). *Chandra* operates using a combination of two charged coupled device (CCD) arrays, the ACIS-Imaging or the ACIS-Spectroscopy (ACIS-I and ACIS-S, respectively), where the focus can be placed on either. The *XMM-Newton* EPIC instrument is composed of three cameras, MOS1, 2 (Turner et al. 2001) and PN (Strüder et al. 2001), which operate simultaneously. *Chandra* observations of A2390 and MACSJ1423.8+2404 are ACIS-S, all the others are ACIS-I.

The *Chandra* observations of the six nearest clusters in Table 1 have previously been analysed in Vikhlinin et al. (2006, 2009a, hereafter V06 and V09) using the CCCP procedure. The corresponding *XMM-Newton* observations were analysed in Planck Collaboration XI (2011) using the REXCESS analysis procedures. These published results are directly compared in Sect. 4.1.

3. Data analysis

Appendix A summarises the basic data reduction, including production of calibrated event files, point source masking and background estimation.

3.1. Effective area correction

To derive the density profile, we needed to convert count rates to emission measure $EM = \int n_e^2 dv$. These quantities are related by the cooling function in the energy band under consideration, $\Lambda(T, Z)$, taking into account the absorption, the redshift, and the instrumental response (i.e. the effective area as a function of energy and position). $\Lambda(T, Z)$ depends on the temperature and metallicity in the region under analysis. The effective areas of *Chandra* and *XMM-Newton* vary across the field of view as a result of different effects, including the non-uniformity of the CCD quantum efficiency, and the telescope vignetting (which reduces the number of photons detected on different portions of the detector). These spatial effects depend on the photon energy, a measure that itself is affected by uncertainty.

As discussed in [Arnaud et al. \(2001\)](#), there are two procedures that are generally used to take into account vignetting effects. The first, which we call the post-correction method, and which was adopted by V06/V09 and in the CCCP analysis, consists of computing the effective area at each position. The area-averaged effective area for each annulus is used to convert the count rate to emission measure along the line of sight.

The second, which we call the pre-correction method ([Arnaud et al. 2001](#); [Churazov et al. 2008](#)), and which was adopted in the REXCESS analysis, first corrects the data for the spatial dependence of the instrument response. For each photon, detected at the position (i, j) and with energy e , a weight $W(i, j, e)$ is assigned such that:

$$W(i, j, e) = \frac{A_{\text{eff}}(i_0, j_0, e)}{A_{\text{eff}}(i, j, e)}, \quad (1)$$

where $A_{\text{eff}}(i, j, e)$ is the effective area computed at the photon position and $A_{\text{eff}}(i_0, j_0, e)$ is the effective area at the aim-point, that is, where it attains its maximum value. The corrected number counts in a given extraction region and energy band is then simply the sum of the weights. This represents the number of photons we would obtain if the detector had a uniform response equivalent to that at the aim-point position.

The pre-correction method was proposed by [Arnaud et al. \(2001\)](#) primarily for spectroscopic analysis in cases when the spatial distribution of the source cannot be considered as uniform across the extraction region. In such cases, the averaging of the effective area over the region under consideration is not trivial and is potentially biased. For surface brightness profile studies, the main advantage of the method is the simplification of the analysis (particularly for the cosmic background subtraction). The main drawback is a statistical degradation as compared to the direct method, by a typical factor of $\sqrt{\langle W^2 \rangle} / \langle W \rangle$, where the brackets denote the average over the extracted photons. However, this degradation is limited as the vignetting variations are small across typical annulus widths and in the soft energy band. We note also that the method is only exact for a perfect knowledge of the photon energy and position. In practice, it requires that the vignetting does not vary significantly within the PSF scale and within the uncertainties on the photon energy (i.e. the spectral resolution). This is the case both for *Chandra* and *XMM-Newton*.

For *XMM-Newton* we computed the weights using the built-in SAS `evigweight` routine. For *Chandra*, which has no built-in function, we have developed a procedure that computes an analogous weight quantity using CIAO tools. The procedure is described in detail in Appendix B. In addition to the weight, for each photon we also computed the exposure time using the

related exposure maps generated for *Chandra* and *XMM-Newton* using the `fluximage` and the `eexpmap` tools, respectively.

To determine the impact of these different vignetting correction techniques, in Sect. 4 we compare the density profiles obtained from the pre-correction method and from the reference V06/V09 profiles calculated with the post-correction procedure.

3.2. Surface brightness profiles

We extracted surface brightness profiles from concentric annuli centred on the X-ray peak in the [0.3–2.5] keV and [0.7–2] keV energy bands from *XMM-Newton* and *Chandra* datasets, respectively. The minimum width of the annuli (3.3'' for *XMM-Newton*; 2'' for *Chandra*) was set in order to ensure a sufficient number of counts in each radial bin and to best exploit the resolution of the instruments. The count rate for each annulus was then computed as the sum of the weights divided by the appropriate exposure time, normalised by the area ([Arnaud et al. 2001](#)). We removed the particle background by extracting the surface brightness profile of the recast CLOSED (*XMM-Newton*) or STOWED (*Chandra*) event lists in the same annular regions, and subtracting these from the source surface brightness profile. We then identified a region free from cluster emission (generally an annulus in the outer regions of the observation) and determined the mean count-rate corresponding to the sky background level. This value was subtracted, and the profile re-binned to have a significance of 3σ per bin, using a logarithmic binning factor of $r_{\text{out}}/r_{\text{in}} = 1.05$.

3.3. Temperature profiles

We undertook the following spectral analysis to estimate temperatures, which are needed to compute the cooling function $\Lambda(T, Z)$. The particle background contribution was removed by subtracting the spectrum extracted from the background datasets in the same detector region. To model the sky background, we extracted the particle-background-subtracted spectrum from the region free of cluster emission defined in Sect. 3.2. We fitted this spectrum with a model consisting of an absorbed (WABS; [Morrison & McCammon 1983](#)) power law with index $\alpha = 1.42$ ([Lumb et al. 2002](#)) for the extra-galactic cosmic X-ray background (CXB) emission, plus two absorbed MEKAL ([Kaastra 1992](#); [Liedahl et al. 1995](#)) models for the Galactic emission ([Kuntz & Snowden 2000](#)). The absorbing column density was fixed to $N_{\text{H}} = 0.7 \times 10^{20} \text{ cm}^{-2}$ ([Parmar et al. 1999](#)) for one of the local Galactic component, and to the 21 cm value (Table 1) for the other two components. The normalisations of all the components and the two MEKAL temperatures were determined from the fit. The sky background model was fixed to its best-fitting parameters and simply scaled to match the geometrical area of the region of interest. We fitted an absorbed MEKAL model, in addition to the fixed sky background model, to estimate the temperature of the ICM. The absorption was fixed to the Galactic line of sight value given Table 1. The abundance was left as a free parameter if the relative error was less than 30%, otherwise it was fixed to 0.3. The fits were performed in the [0.7–10] keV and [0.3–11] keV bands for *Chandra* and *XMM-Newton*, respectively. For the *XMM-Newton* fit, we also excluded the [1.4–1.6] keV band for all three cameras and the [7.45–9.0] keV band for PN only (see e.g. [Pratt et al. 2007](#)) to avoid prominent instrumental emission lines. All the models considered in the spectral analysis were convolved by the appropriate response functions. For *Chandra* the response matrix

Table 2. Gas masses computed at fixed radii. Here R_{500, Y_X} is measured via the $M_{500}-Y_X$ relation, using the *XMM-Newton* datasets.

Cluster name	R_{500, Y_X} [kpc]	$M_{\text{gas}} (R < R_{2500})$			$M_{\text{gas}} (R < R_{500})$				
		XMM	CXO	XMM PXI	CXO V06/V09	XMM	CXO	XMM PXI	CXO V06/V09
		[$10^{13} M_{\odot}$]			[$10^{13} M_{\odot}$]				
A1651	1132^{+9}_{-9}	2.01 ± 0.01	2.10 ± 0.01	2.10 ± 0.04	2.03 ± 0.01	5.61 ± 0.05	6.05 ± 0.07	6.11 ± 0.07	5.61 ± 0.08
A1650	1114^{+4}_{-4}	1.81 ± 0.00	1.87 ± 0.01	1.83 ± 0.02	1.84 ± 0.00	5.16 ± 0.02	5.11 ± 0.06	5.26 ± 0.06	5.13 ± 0.03
A1413	1233^{+4}_{-4}	2.86 ± 0.01	2.97 ± 0.01	2.90 ± 0.03	2.88 ± 0.01	7.87 ± 0.03	7.89 ± 0.05	8.02 ± 0.05	8.09 ± 0.02
A2204	1348^{+12}_{-12}	4.01 ± 0.02	4.22 ± 0.01	4.07 ± 0.03	4.04 ± 0.02	10.94 ± 0.12	11.54 ± 0.08	11.49 ± 0.08	10.96 ± 0.13
A2163	1787^{+6}_{-6}	10.17 ± 0.02	10.42 ± 0.03	10.41 ± 0.09	9.92 ± 0.04	32.63 ± 0.09	34.12 ± 0.14	31.26 ± 0.13	32.14 ± 0.27
A2390	1441^{+14}_{-12}	5.85 ± 0.03	6.04 ± 0.02	5.57 ± 0.05	5.88 ± 0.03	15.50 ± 0.12	16.54 ± 0.09	15.86 ± 0.09	15.90 ± 0.15
MACS J1423.8+2404	981^{+12}_{-13}	2.22 ± 0.03	2.39 ± 0.02	-	-	6.31 ± 0.09	6.74 ± 0.08	-	-
MACS J0717.5+3745	1307^{+12}_{-11}	5.72 ± 0.03	5.83 ± 0.05	-	-	19.62 ± 0.12	19.29 ± 0.27	-	-
MACS J0744.9+3927	1032^{+10}_{-11}	3.44 ± 0.03	3.60 ± 0.05	-	-	10.69 ± 0.11	10.70 ± 0.19	-	-
SPT-CL J2146-4633	737^{+12}_{-13}	1.00 ± 0.01	1.02 ± 0.03	-	-	4.73 ± 0.05	4.84 ± 0.18	-	-
SPT-CL J2341-5119	769^{+14}_{-14}	1.69 ± 0.02	1.73 ± 0.04	-	-	5.12 ± 0.08	5.19 ± 0.18	-	-
SPT-CL J0546-5345	782^{+17}_{-14}	1.71 ± 0.02	1.82 ± 0.06	-	-	5.87 ± 0.09	6.15 ± 0.21	-	-

file (RMF) and the ancillary response file (ARF) were computed using the CIAO `mkacisrmf` and `mkarf` tools, respectively. The same was done for *XMM-Newton*, using the SAS tools `rmfgen` and `arfgen`.

To determine the projected (2D) temperature profile, we extracted spectra from concentric annular regions centred on the X-ray peak, each annulus being defined to have $r_{\text{out}}/r_{\text{in}} = 1.3$ and a signal-to-noise ratio (S/N) of at least 30. After instrumental background subtraction, each spectrum was rebinned to have at least 25 counts per bin. We were able to measure a temperature profile for the nine lowest-redshift objects both for the *Chandra* and the *XMM-Newton* samples.

3.4. Density and gas mass profiles

We considered two different techniques to derive the radial (3D) density profiles from the X-ray surface brightness: parametric modelling, and non-parametric deconvolution and deprojection. The non-parametric deconvolution technique with regularisation is that proposed by Croston et al. (2006), which was used throughout the REXCESS analysis. Hereafter, we refer to this method as the deprojection technique, and refer to the derived density profiles from this analysis as the deprojected density profiles. Briefly, the observed surface brightness profile, C_{obs} , can be modelled as the result of the emission produced by the hot plasma in concentric shells, S_{emit} , projected along the line of sight, and convolved with the instrument PSF:

$$[C_{\text{obs}}] = [R_{\text{PSF}}][R_{\text{proj}}][S_{\text{emit}}], \quad (2)$$

where R_{proj} and R_{PSF} are the projection and PSF matrices, respectively. The method consists of inverting Eq. (2), and using regularisation criteria to avoid noise amplification (see Croston et al. 2006, for details). We used the analytical model described in Ghizzardi (2001) for the *XMM-Newton* PSF. For our purposes the *Chandra* PSF can be neglected since the annuli used to perform imaging and spectroscopic analysis are far larger than the *Chandra* PSF over the entire radial range under consideration. We thus assumed an ideal PSF, that is, the R_{PSF} for *Chandra* datasets is the unity matrix. The projection matrix R_{proj} was evaluated assuming that the emission comes from concentric spherical shells, each with constant density. The recovered density in the shell is thus the square root of the mean density squared. The contribution from shells external to the maximum radius used for the surface brightness profile extraction was removed by modelling the deprojected surface brightness emission in the external

regions with a power law. The deprojection matrix is purely geometrical and is the same for both *Chandra* and *XMM-Newton* datasets. Individual deprojected density profiles derived from the *Chandra* and *XMM-Newton* datasets are shown in the upper panels of Fig. C.1.

We also derived the density profile using the parametric modified- β model described in Vikhlinin et al. (2006), which we refer to hereafter as the parametric fit technique (the corresponding density profiles will be referred as parametric density profiles). Parameters were estimated through a fit of the observed surface brightness profile with a projected analytical model, convolved with the PSF. For clarity, in the figures, profiles have the suffix `dep` and `par`, depending on whether the deprojection or parametric technique has been used.

The errors were computed from 1000 Monte Carlo realisations of the surface brightness. Unless otherwise stated, the cooling function profile used to convert to density was determined from the 2D temperature profile. For the three most distant clusters, the observation depth does not allow the determination of the temperature profile, so we used a constant temperature measured in the region that maximises the signal to noise.

We obtained gas mass profiles by integrating the deprojected density profiles in spherical shells. These are shown in Fig. C.2 for both the *Chandra* and *XMM-Newton* datasets, respectively. We determined R_{500} iteratively using the $M_{500}-Y_X$ relation of Arnaud et al. (2010), where Y_X is the product of T_X , the temperature measured within $[0.15-0.75]R_{500}$, and $M_{\text{gas},500}$ (Kravtsov et al. 2006). Gas masses were calculated within this same aperture for both *XMM-Newton* and *Chandra* datasets. The corresponding values are reported in Table 2. While in principle we could use the hydrostatic mass profiles to obtain R_{500} we choose instead the Y_X proxy. This is expected to be more robust to the presence of dynamical disturbance (e.g. Kravtsov et al. 2006) and allows us to obtain homogeneous mass estimates in the presence of lower quality data, that is, high- z objects.

4. Robustness of density profile reconstruction

In the following we compare individual profiles by computing their ratio, after interpolation onto a common, regular grid in log-log space. We computed a ‘‘mean’’ ratio profile by taking either the median or the error weighed mean, and also calculated the 68% confidence envelope. The two averaging methods give consistent results, and the results quoted below are defined with respect to the median profile.

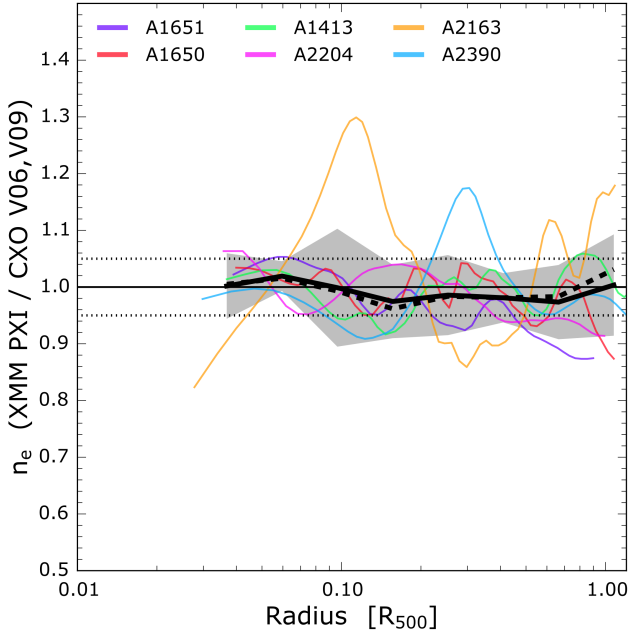


Fig. 1. Ratio of *XMM-Newton* and *Chandra* gas density profiles published by Vikhlinin et al. (2006, 2009a) and Planck Collaboration XI (2011; PXI), obtained using independent analysis techniques. The *XMM-Newton* and the *Chandra* profiles are derived from deprojection and parametric model fitting, respectively. The vignetting correction method is different (see text). The point source and substructure masking and centre choices are also independent. The black solid (dashed) line represents the median (weighted mean) and the grey shaded area its 1σ confidence level. The dotted horizontal lines represent the $\pm 5\%$ levels. At large scale the profiles show good agreement in the shape, with an average offset of $\sim 2\%$. In the inner regions differences are dominated by the choice of the centre. The difference between the centres ranges from 1 to ~ 14 arcsec ($< 0.02 R_{500}$ in all cases).

4.1. First comparison

Figure 1 presents the ratio between the deprojected *XMM-Newton* density profiles obtained using the REXCESS method and published by Planck Collaboration XI (2011), and the *Chandra* parametric profiles obtained using the CCCP method and published in V06. These are completely independent measurements, both in terms of instruments and methods. We recall that the REXCESS analysis is based on photon weighting for vignetting correction, and deprojection of the surface brightness profiles. In the CCCP analysis, the emission measure profiles, obtained after conversion of the observed count rate using the instrument response at each radius, are fitted with a general parametric model. The excluded point sources, the profile extraction centre, and substructure masking are those of the original published works (Planck Collaboration XI 2011, V06/V09), and are thus also independent. For a correct comparison when comparing the *XMM-Newton* profiles to V06/V09, we masked the contribution from the inner 40 kpc as was done in these works.

This first comparison provides an initial test of the robustness of the density profile reconstruction in general, and is representative of the maximum variation we can expect using different instruments, data, and profile extraction analysis. The overall consistency between the profiles is good: as shown by the shaded envelope, they agree to better than 5% on average across the full radial range. The largest outlier is A2163, a complex object

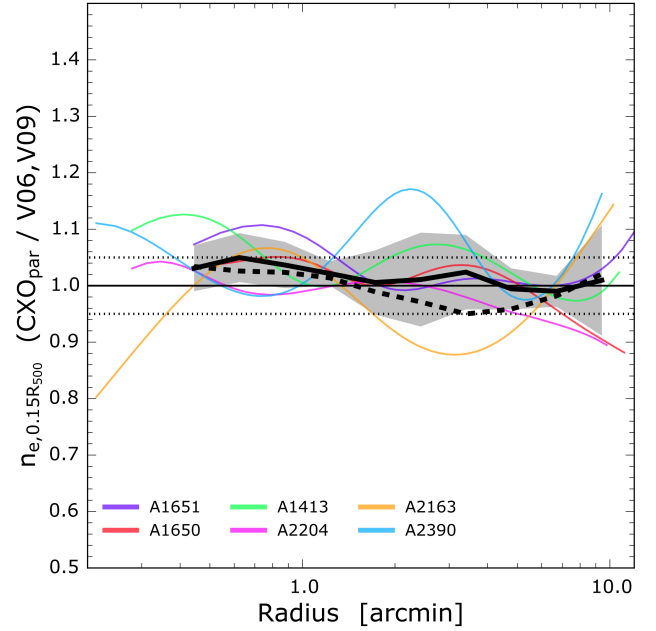


Fig. 2. Test of the *Chandra* photon weighting implementation developed in the present paper (Sect. 3.1 and Appendix B). The Figure shows the ratio between the parametric *Chandra* density profiles derived with the weighting method developed here (pre-correction) and those published in V06/V09 (post-correction). Profiles are scaled by $n_{e,0.15 R_{500}}$ to compare the shape. Legend as for Fig. 1. Also as for Fig. 1, deviations in the core ($r < 0.5'$) are due to the different centres used for profile extraction.

for which profile reconstruction is particularly sensitive to the masking of substructures and the choice of centre, which are different in the two works we compare here. Above $0.1 R_{500}$ the profiles have similar forms, the ratio being almost constant. The median ratio suggests a small normalisation offset, the *Chandra* profiles being $\sim 2\%$ higher than *XMM-Newton*, although both instruments give consistent measurements within the errors. We conclude that such completely independent analyses, using very different methods, may result in differences in absolute density values of the order of a few percent. We now undertake a number of further tests designed to investigate the impact on the density profiles of various data treatment choices and assumptions.

4.2. Tests of effective area correction method

As described in Sect. 3.1, the effective area correction can be performed after profile extraction using the local effective area (post-correction), or by weighting the photons before profile extraction (pre-correction). To investigate the impact of the different methods, and to validate the weighting procedure we developed here for *Chandra* data, we compare the *Chandra* parametric density profiles derived with the weighting method for the six nearby clusters to those published in V06/V09. To account for possible effects introduced by using different versions of the CALDB, we normalised the profiles by the density computed at $0.15 R_{500}$. Figure 2 shows that the agreement in profile shapes is remarkably good: the median ratio has maximum variations of the order of $\sim 1\%$ around unity. As in Fig. 1, the profiles differ in the centre, sometimes by large amounts, simply because different centres have been used for the profile extraction. The absence of evident biases or trends with increasing off-axis angle implies that the weighting correction technique does not introduce any

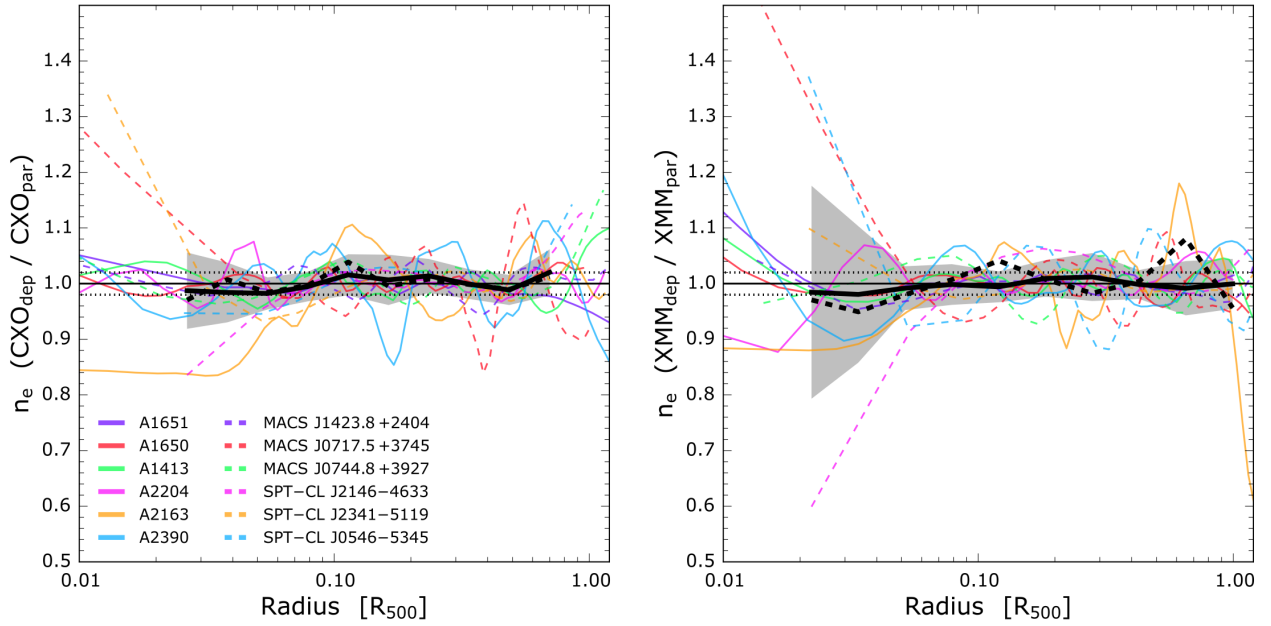


Fig. 3. Test of parametric vs. deprojection methods. *Left panel:* ratio between the *Chandra* density profiles obtained using the deprojection and parametric fit techniques. All other aspects of the analysis are identical. Legend as in Fig. 1 except that the dotted lines represent $\pm 2\%$ levels here. *Right panel:* same as in the left panel, but for the *XMM-Newton* density profiles.

systematic uncertainties into the analysis. There is a large dispersion in the $\sim 8\text{--}9$ arcmin region. This is due to the fact that most of the annuli in this region reach the border of the ACIS chips, where we expect poor count rates and hence noisy measurements. Given the good agreement discussed above, in the following, all further tests will be undertaken on profiles extracted with the photon weighting (pre-correction) method.

4.3. Tests of parametric versus non-parametric methods

In this section we test the robustness of the reconstruction to the method used to derive (3D) density profiles from the projected data. Figure 3 shows the comparison between the density profiles derived using the deprojection method to those derived from parametric fitting. The ratios are shown for the *Chandra* and *XMM-Newton* sample in the left and right panels, respectively. In both cases there is an excellent agreement above $0.02 R_{500}$, the median value being close to one, and the uncertainty envelope being of the order of $\sim 1\%$. There are strong deviations in the inner parts of the *XMM-Newton* sample and a larger scatter in the central parts of both datasets. This is probably related to the presence of disturbed clusters, for which the parametric model has a tendency to smooth the variations of the surface brightness profiles. In the following, all further tests will be undertaken on profiles extracted with the non-parametric (deprojection) method.

4.4. Impact of temperature profiles

As explained in Sect. 3.3, density profile reconstruction relies on the cooling function, $\Lambda(T)$, used to convert count rates to emission measure profiles. We first investigated the impact of the offset between *Chandra* and *XMM-Newton* temperature measurements. We expected the effect to be small, as the cooling function depends only weakly on temperature at the typical energies used for surface brightness extraction, $\sim [0.5\text{--}2]$ keV. For

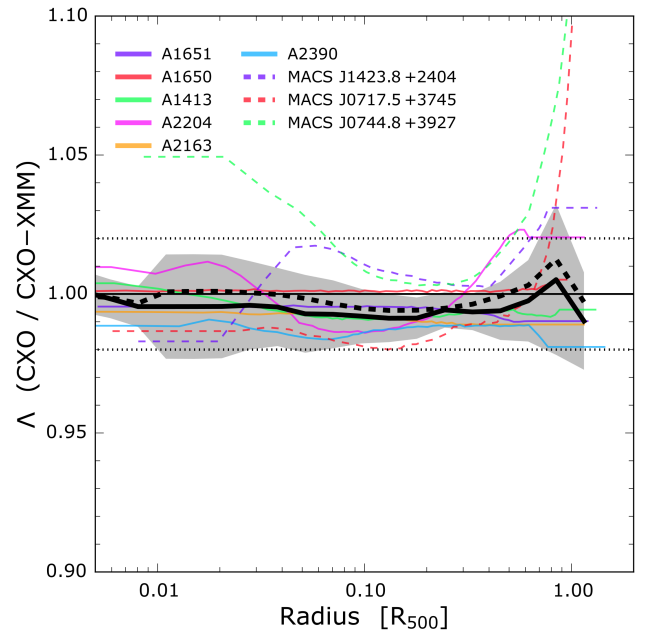


Fig. 4. Effect of systematics on temperature profiles. Ratio of $\Lambda(T)$ profiles derived for *Chandra* data, using the temperature profiles measured by *Chandra* and *XMM-Newton*. The $z > 0.9$ clusters are excluded as the *Chandra* observations are not sufficiently deep for temperature profiles to be measured. The legend is the same as in Fig. 1 except that horizontal dotted lines represent $\pm 2\%$ levels.

each *Chandra* profile, we computed the $\Lambda(T)$ profile using the *XMM-Newton* temperature profiles, namely $\Lambda_{\text{CXO-XMM}}$. In Fig. 4, these profiles are compared to the nominal profiles computed from the *Chandra* temperature profile, Λ_{CXO} . Over the full radial range the profiles show an agreement within 1%. Comparing density profiles reconstructed using Λ_{CXO} and

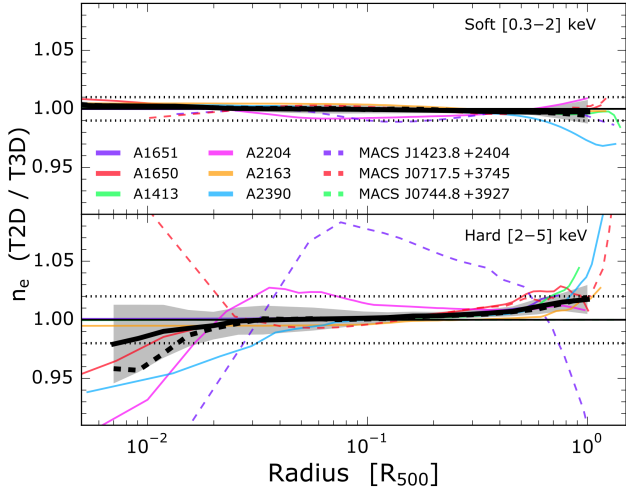


Fig. 5. Ratio between the density profiles obtained using 2D and 3D temperature profiles. *Top panel:* The density profiles are derived from the *XMM-Newton* surface brightness extracted in the [0.3–2] keV energy band. The effect of using 2D profiles is negligible. The three highest redshift clusters, shown with dotted lines, are not included in the computation of the median, mean and their dispersion (see text for details). *Bottom panel:* profiles are obtained from surface brightness profiles extracted in the [2–5] keV band. Here it is important to use 3D profiles since the surface brightness is particularly sensitive to the temperature. Legend as in Fig. 1 except that horizontal dotted lines represent the $\pm 2\%$ levels. As in the upper panel, the three highest redshift clusters are not included in the computation.

$\Lambda_{\text{CXO-XMM}}$ yields differences of the order of $<0.5\%$. Thus the offset in temperature measurements between *XMM-Newton* and *Chandra* does not affect density profile reconstruction.

The $\Lambda(T)$ function is nominally computed using the projected (2D) temperature profile. In principle the emissivity should be computed in each shell, that is, using the 3D temperature profile. It may differ from the 2D profile in the case where there are large temperature gradients, such as in the centres of cool core clusters. We derived the 3D temperature profile from a parametric fit of the 2D profile, using the weighting scheme introduced by Mazzotta et al. (2004) and Vikhlinin (2006) to correct for spectroscopic bias. The average temperature in each annulus was computed from the contribution of each shell, taking into account the projection and PSF geometrical factors, and applying a density- and temperature-dependent weight, as defined by Vikhlinin (2006). This process is in principle iterative, as the 3D temperature profile depends on the density profiles via the weights, while the density depends on the temperature via the cooling function. In practice, we did not iterate the process, the final correction being very small.

To study the impact of using 2D rather than 3D temperature profiles, we examined the ratio of the density profiles computed with the corresponding 2D and 3D cooling functions. The density profiles are generally derived from the soft band surface brightness because of the higher S/N and the decreasing temperature dependence of the emissivity with energy. However, the emissivity depends on the *effective* temperature $kT_{\text{eff}} = kT/(1+z)$, so that the soft band in fact behaves equivalently to the hard band for sufficiently high z clusters (e.g. $kT_{\text{eff}} < 2$ keV). In Fig. 5 we thus show the profile ratios obtained in both the soft ([0.3–2] keV) and hard ([2–5] keV) energy bands. As expected, the density profiles of the low redshift sample, derived from soft energy band data, are perfectly consistent, well within 1%, as

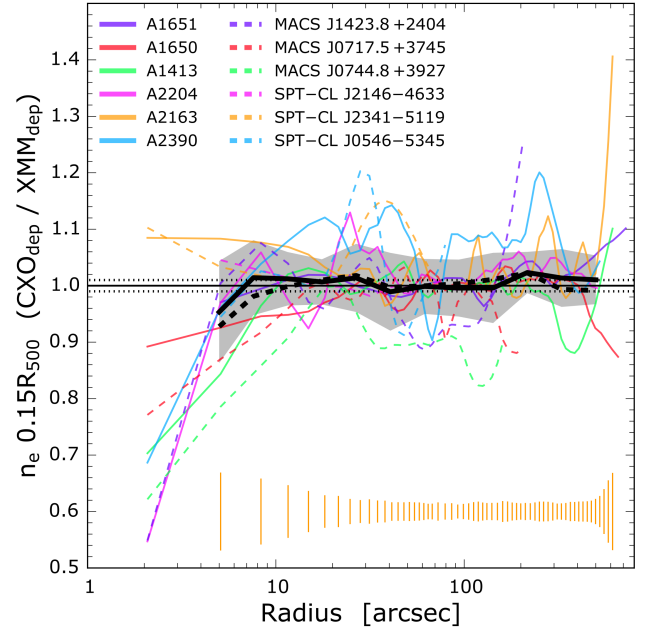


Fig. 6. Test of the *XMM-Newton* PSF correction in the soft energy band: ratio between normalised density profiles obtained from the deprojection of *Chandra* and *XMM-Newton* surface brightness profiles. The error bars correspond to the error on the A2163 profile, and represent the typical uncertainties as a function of radius. Each profile is normalised by the density computed at $R = 0.15 R_{500}$ to assess shape differences. There is an excellent agreement between the profile shape above $5''$, showing that the *XMM-Newton* PSF is properly accounted for in the density reconstruction. Legend as in Fig. 1 except that horizontal dotted lines represent $\pm 1\%$ levels.

the dependency of the emissivity on the temperature is extremely weak at low energies. For the three clusters at $z > 0.25$ with temperature profiles, the effective temperature remains above 2 keV, and there is indeed good agreement between the 2D and the 3D results. However, with increasing redshifts the spectrum is shifted to lower energies, and the exponential cut off may reach the soft band used to extract the profiles and a full 3D analysis may become necessary. Unfortunately, for the three clusters at $z \sim 1$ the observation depth is insufficient to determine their temperature profiles so that this point cannot directly be assessed. We did find significant differences in the hard band, that become important for clusters with a complex morphology or strong cool core clusters (such as A2204). For this reason, one needs to use the 3D temperature profiles when deprojecting hard band surface brightness, or high z clusters, particularly at low temperature.

4.5. Tests of the *XMM-Newton* PSF correction

One crucial point of the density profile reconstruction is the correct estimation of the $[R_{\text{PSF}}]$ term and the corresponding correction of the PSF effect. This effect is only important for *XMM-Newton*, for which the PSF¹ has a full width at half-maximum (FWHM) $\sim 6''$ and a half-energy-width (HEW) $\sim 15''$. This PSF size becomes particularly important for high redshift clusters. Typical R_{500} values for a $z \sim 1$ cluster are of the order of $\sim 1\text{--}2$ arcmin; a resolution of $6''$ at the same redshift corresponds to 56 kpc for the cosmology we assume here. We thus exploited

¹ Values taken from the *XMM-Newton* User's Handbook.

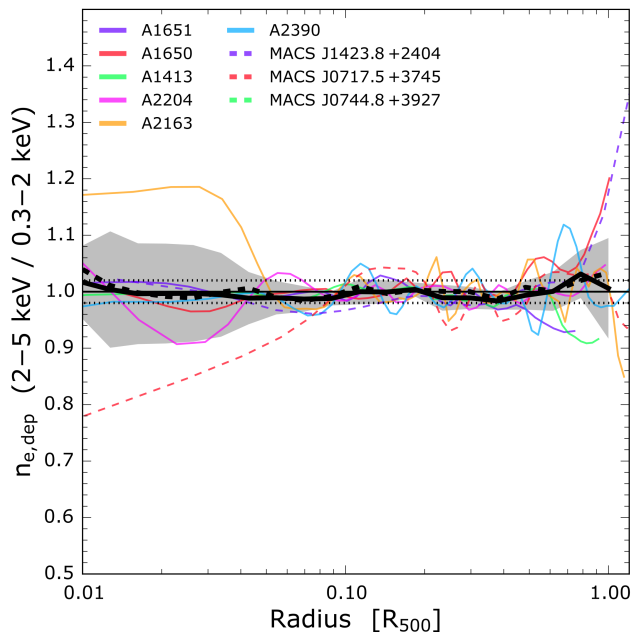


Fig. 7. Test of the *XMM-Newton* PSF correction in the hard energy band. Comparison between the deprojected density profile obtained from the *XMM-Newton* surface brightness profiles extracted in the [0.3–2] keV and in the [2–5] keV band. Legend is the same as in Fig. 1 except that dotted lines represent $\pm 2\%$ level.

the excellent resolution of *Chandra* to undertake a set of tests to probe the robustness of the *XMM-Newton* PSF model.

4.5.1. Test of the *XMM-Newton* PSF correction at low energy

As a first test, we investigated if the PSF is properly corrected for in the [0.3–2] keV energy range we use to extract the *XMM-Newton* surface brightness profiles. In Fig. 6 we compare the *Chandra* and *XMM-Newton* density profiles rescaled by the respective n_e computed at $0.15 R_{500}$. Above $\sim 6''$ the profiles are in excellent agreement, the median values scattering around unity with oscillations of the order of 0.5%. That is, in the energy range under consideration, the $[R_{\text{PSF}}]$ term accurately reproduces the behaviour of the *XMM-Newton* PSF. Density profile reconstruction is thus robust to the *XMM-Newton* PSF down to the resolution of its typical FWHM. For a cluster of $M_{500} = 4 \times 10^{14} M_{\odot}$ at $z = 1$, this resolution limit corresponds to typical scales of $R/R_{500} \sim 0.07$. Below $\sim 6''$, the dispersion increases and the *XMM-Newton* profiles appear too peaked on average. Here we are entering the very core of the *XMM-Newton* PSF, where the spatial information is lost.

4.5.2. Test of the energy dependence of the *XMM-Newton* PSF

As a by-product of this analysis we were also able to investigate whether the *XMM-Newton* PSF correction is also accurate at high energy. Knowledge of the energy dependence is crucial for derivation of the temperature profile, the temperature measurement relying on the full energy band. For instance, incomplete knowledge of the *XMM-Newton* PSF has been suggested as an explanation for the difference in the temperature profile shape obtained with *XMM-Newton* and *Chandra* by Donahue et al. (2014). Figure 7 shows the comparison between the density

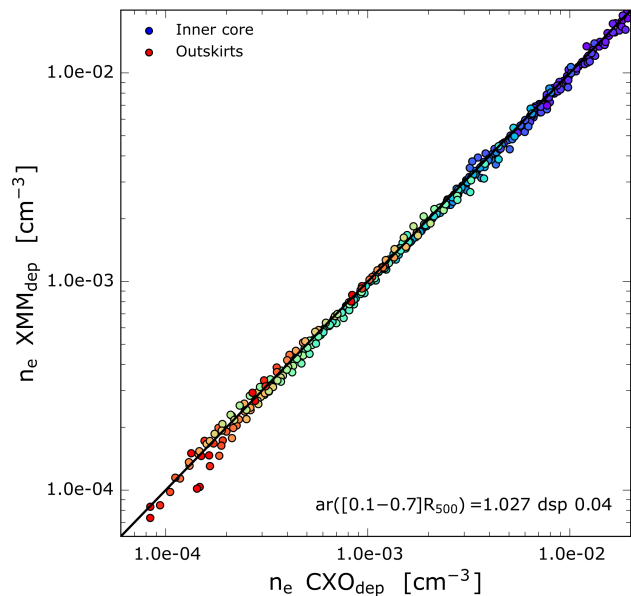


Fig. 8. Deprojected *XMM-Newton* and *Chandra* densities. Points are colour coded according to the rainbow table to help the reader identify the inner and outer regions of the cluster, plotted with red and blue, respectively. The black solid line represents the identity relation. The average ratio between all the profiles in the $[0.1-0.7] R_{500}$ region is 1.027 with a dispersion (dsp) of 0.04.

profiles obtained using the hard and soft band surface brightness, where for the hard band we use 3D temperature profiles to compute the cooling function (see Sect. 4.4 above). The agreement is remarkably good, the median ratio profile presenting oscillations of maximum 2% around unity. There is a large dispersion in the central regions, which is driven by the presence of clusters with a complex morphology such as A2163 and MACS J0717. However, above $0.1 R_{500}$ the 1σ dispersion remains within $\pm 10\%$ (and within $\pm 2\%$ below $0.6 R_{500}$). From this test we conclude that the model of *XMM-Newton* PSF also correctly reproduces the correct behaviour as a function of energy.

4.6. Absolute density comparison

As already shown in Fig. 6, the agreement in density profile shape between the instruments is excellent. We now focus on the flux differences, that is, differences in terms of absolute normalisation. Figure 8 shows the scatter plot between all the data points from the *Chandra* and *XMM-Newton* profiles. The analysis method is the same for both observatories, and is based on the photon weighting method and non-parametric deprojection of the surface brightness profiles. We colour-code the points following the rainbow table to clearly identify the inner, higher density, and the outer, lower density regions. Focussing on the $[0.1-0.7] R_{500}$ region, we clearly see the presence of an offset, with the average ratio of all the values in this region yielding 1.027 with a dispersion of 0.04%. This value is in agreement with previous work by Martino et al. (2014) and Donahue et al. (2014), and is consistent with unity over the radial range under consideration.

Inspection of individual cluster profiles in Fig. C.1 reveals that the normalisation offset presents complex behaviour. While A2204, A1413, A2390, and the three MACS clusters present a clear offset, the other clusters show good agreement, including in terms of normalisation. The normalisation offset thus seems

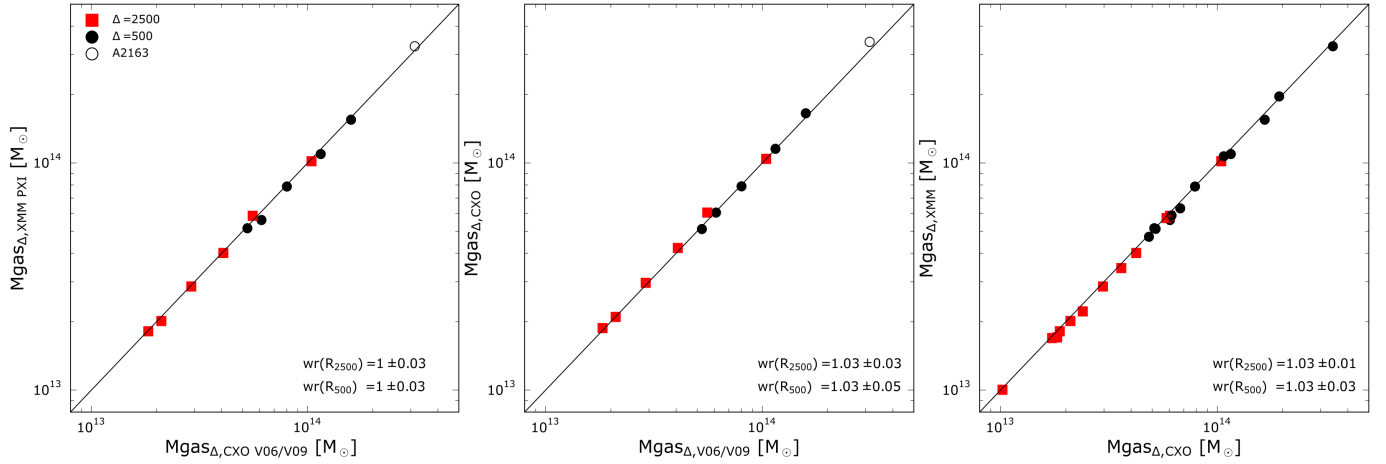


Fig. 9. Ratios between the integrated gas masses within R_{2500} and R_{500} obtained from the *XMM-Newton* and the *Chandra* data. For all panels: the solid line represents the identity relation. *Left panel:* *XMM-Newton* gas masses obtained by Planck Collaboration XI (2011; PXI) vs. *Chandra* gas masses from Vikhlinin et al. (2006, 2009a). *Central panel:* *Chandra* gas masses derived from the pre-correction (photon weighting) method compared to those published in V06/V09. *Right panel:* *XMM-Newton* and *Chandra* gas masses obtained using the same analysis method (photon weighting method and non-parametric deprojection of the surface brightness profiles).

to depend also on individual cluster observations, with a general trend for *Chandra* fluxes being slightly higher. This may reflect a dependence on observation conditions (e.g. residual soft proton contamination), or on observing epoch (if the calibration does not follow perfectly the instrument evolution). It may also depend on intrinsic cluster properties, for example a physical effect such as clumpiness, whose impact on the final density value may depend on the instrument sensitivity in the extraction band.

5. Consequences for the gas mass

Gas mass is a fundamental quantity used to characterise galaxy clusters. Together with the stellar mass it yields the total amount of baryons, and if the total cluster mass is known, one can calculate the baryon fraction. The latter can be used for cosmological studies (see e.g. Sasaki 1996; Pen 1997; Vikhlinin et al. 2009b; Mantz et al. 2014). The quantity Y_X , the product of the gas mass and the temperature introduced by Kravtsov et al. (2006), is a low scatter proxy heavily used for the total cluster mass. It is the analogue of the integrated Compton parameter Y , thus linking X-ray and microwave based observations. For these reasons, it is fundamental to investigate the impact of different analysis techniques, and of the normalisation offset, on the gas mass profile reconstruction and the total gas masses derived from these. In particular, $M_{\text{gas},\Delta}$ computed at $\Delta = 2500, 500$ are of notable importance².

Figure 9 shows the gas mass computed at $R = R_{2500}$ and $R = R_{500}$. We show three comparisons, corresponding to the tests performed in Sects. 4.1, 4.2, and 4.6 respectively, viz.

- The left panel shows the scatter plot between the gas masses independently derived by Planck Collaboration XI (2011) and by Vikhlinin et al. (2006, 2009a). We recall that the former are derived from *XMM-Newton* data using the pre-correction (photon weighting) method and using deprojection of the surface brightness profiles. The latter are obtained

from *Chandra* data using the post-correction method and parametric gas density profile models. There is remarkably good agreement at R_{2500} , the weighted ratio of this subsample yielding $WR_{2500} = 1.00 \pm 0.03$. The agreement is also good when considering the R_{500} subsample. The corresponding weighted ratio is $WR_{500} = 1.00 \pm 0.03$.

- The central panel tests the impact of the vignetting correction method. The *Chandra* gas masses obtained using the pre-correction (photon weighting) method are compared to the values published in V06/V09. There is no evident trend or behaviour, as all the points are aligned with the 1:1 slope. Computing a weighted ratio at R_{2500} yields $WR_{2500} = 1.03 \pm 0.03$. This value confirms the presence of the offset, due to the different calibration files used between the V06/V09 analysis and the analysis presented in this paper. Removing A2163 does not change the result. At R_{500} the weighted ratio is $WR_{500} = 1.03 \pm 0.03$ considering A2163; removing this cluster yields $WR_{500} = 1.01 \pm 0.03$. This result again confirms the excellent agreement between measurements performed using completely independent analyses.
- Finally, the right panel compares the *XMM-Newton* and *Chandra* gas masses obtained using the same analysis method (pre-correction and non-parametric deprojection, in both cases). Both subsamples show the same behaviour, all the points being slightly below the unity line. This result is confirmed by the weighted ratios $WR_{2500} = 1.03 \pm 0.01$ and $WR_{500} = 1.03 \pm 0.03$. In this case A2163 is less problematic because in this comparison the X-ray peaks on which we centre our profiles are the same. *Chandra* gas masses are slightly higher, though consistent, with those from *XMM-Newton*.

6. Discussion and conclusions

In this work we have compared the gas density profiles and integrated gas masses obtained from *Chandra* and *XMM-Newton* observations for a sample of 12 clusters. We have undertaken a

² $R_{2500} \approx 0.45 R_{500}$.

thorough investigation of potential sources of systematic differences between measurements, taking into account that the data originate from different observatories, and examining subtle effects linked to the analysis method used to reconstruct the gas density. We summarise the results of each test in Sect. 3.

Our main conclusions are as follows:

- Direct comparison of previously-published results, obtained from *Chandra* for the CCCP project (Vikhlinin et al. 2006, 2009a) and from *XMM-Newton* for *Planck* studies (Planck Collaboration XI 2011), yield excellent agreement. The differences for individual objects remain within $\pm 5\%$ at any radius, except for very specific features, and there are no obvious systematic trends. This is remarkable, given the different instruments, treatment of instrumental effects such as vignetting, deprojection methods (parametric versus non parametric), and even the point source masking, choice of centre, background subtraction etc.
- For *Chandra*, we implement and validate the event weighting procedure to correct for vignetting before profile extraction, finding similar results to methods that correct a posteriori the surface brightness profiles using the local effective area.
- Density profile reconstruction using parametric fitting of projected profiles (emission measure or surface brightness), or deprojection techniques, show on average an exquisite agreement (better than 1% on average). However, individual fluctuations at various radii can reach up to 10%, linked to the different sensitivity of the reconstruction techniques to small scale surface brightness features, and to the underlying dynamical state of the object in question.
- There is a nearly perfect consistency of the shapes of *Chandra* and *XMM-Newton* density profiles beyond $\sim 6''$ (i.e. the very core of the *XMM-Newton* PSF). Our understanding of the *XMM-Newton* PSF is thus excellent. Further checks show that we are also able to accurately correct for the PSF at high energy. Insufficient knowledge of the *XMM-Newton* PSF was suggested by Donahue et al. (2014) to at least partly account for the differences in the radial temperature profiles they derived from *XMM-Newton* and *Chandra*. Our result does not support this view.
- The known temperature offset between *Chandra* and *XMM-Newton* has almost no impact (less than 0.5%) on the resulting density profile. The approximation made by using the projected (2D) temperature profile to convert count rate to density is negligible in the soft energy band, even in the case of strong temperature gradients, for example cool cores. However when working in the hard band, or equivalently in the soft band but for very high redshift systems, it is essential to account for the deprojected radial temperature profile.
- The overall normalisation offset remains within $\sim 2.5\%^3$. This effect is dominated by the absolute flux calibration, which can depend on the calibration data base version. A second order effect is the dependence on individual observations, linked to cluster properties and/or observation conditions and/or instrument evolution.
- Gas mas profiles generally follow the same behaviour as the density. Gas masses at R_{500} or R_{2500} present a small offset, but on the average the measurements are consistent within 1σ .

³ On average we find a small, though not significant at the 1σ level, offset between the absolute value of the *Chandra* and *XMM-Newton* density profiles, the former being higher on average by 1.027 with a dispersion of 0.04.

Our analysis confirms the good agreement generally found in the literature (e.g. Martino et al. 2014; Donahue et al. 2014), for comparisons of density profiles obtained with *XMM-Newton* and *Chandra* on specific samples analysed with a given procedure. Our study provides a more complete understanding of the different sources of systematic effects, across the full cluster population. The present sample was specifically chosen to cover a wide redshift range (from the local universe to $z \sim 1$), and to sample the variety of dynamical states (from relaxed objects to violent mergers). We address both instrumental effects, by comparing between satellites, and the effect of differing analysis methods, by comparing results obtained from the same satellite and varying the analysis. We emphasise that, on average, the density profiles are robust to the analysis method (e.g. vignetting correction, parametric versus non parametric modelling of the surface brightness); that the effect of the *XMM-Newton* PSF is well understood and can be corrected at small radii deep into the cluster core; and that the overall density normalisation offset remains within $\sim 2.5\%$. The results presented here are important in the context of any project that envisions the combination of *Chandra* and *XMM-Newton* data, and underline the complementarity that such observations afford.

Acknowledgements. The authors thank the referee for his/her comments. The scientific results reported in this article are based on data obtained from the *Chandra* Data Archive and observations obtained with *XMM-Newton*, an ESA science mission with instruments and contributions directly funded by ESA Member States and NASA. The research leading to these results has received funding from the European Research Council under the European Union's Seventh Framework Programme (FP7/2007-2013) ERC grant agreement No. 340519. M.A., P.M., E.P., and G.W.P. acknowledge partial funding support from NASA grant NNX14AC22G. F.A.-S. acknowledges support from *Chandra* grant GO3-14131X.

References

- Allen, S. W., Evrard, A. E., & Mantz, A. B. 2011, *ARA&A*, 49, 409
- Arnaud, M., Neumann, D. M., Aghanim, N., et al. 2001, *A&A*, 365, L80
- Arnaud, M., Pratt, G. W., Piffaretti, R., et al. 2010, *A&A*, 517, A92
- Bartalucci, I., Mazzotta, P., Bourdin, H., & Vikhlinin, A. 2014, *A&A*, 566, A25
- Bartalucci, I., Arnaud, M., Pratt, G. W., et al. 2017, *A&A*, 598, A61
- Churazov, E., Forman, W., Vikhlinin, A., et al. 2008, *MNRAS*, 388, 1062
- Croston, J. H., Arnaud, M., Pointecouteau, E., & Pratt, G. W. 2006, *A&A*, 459, 1007
- Croston, J. H., Pratt, G. W., Böhringer, H., et al. 2008, *A&A*, 487, 431
- Donahue, M., Voit, G. M., Mahdavi, A., et al. 2014, *ApJ*, 794, 136
- Freeman, P. E., Kashyap, V., Rosner, R., & Lamb, D. Q. 2002, *ApJS*, 138, 185
- Fruscione, A., McDowell, J. C., Allen, G. E., et al. 2006, in *SPIE Conf. Ser., Proc. SPIE*, 6270, 62701V
- Garmire, G. P., Bautz, M. W., Ford, P. G., Nousek, J. A., & Ricker, Jr., G. R. 2003, in *X-Ray and Gamma-Ray Telescopes and Instruments for Astronomy*, eds. J. E. Truemper, & H. D. Tananbaum, *Proc. SPIE*, 4851, 28
- Ghizzardi, S. 2001, XMM-SOC-CAL-TN-0022
- Giacconi, R., Rosati, P., Tozzi, P., et al. 2001, *ApJ*, 551, 624
- Hickox, R. C., & Markevitch, M. 2006, *ApJ*, 645, 95
- Kaastra, J. S. 1992, An X-Ray Spectral Code for Optically Thin Plasmas (Internal SRON-Leiden Report, updated version 2.0)
- Kalberla, P. M. W., Burton, W. B., Hartmann, D., et al. 2005, *A&A*, 440, 775
- Kravtsov, A. V., Vikhlinin, A., & Nagai, D. 2006, *ApJ*, 650, 128
- Kuntz, K. D., & Snowden, S. L. 2000, *ApJ*, 543, 195
- Liedahl, D. A., Osterheld, A. L., & Goldstein, W. H. 1995, *ApJ*, 438, L115
- Limousin, M., Richard, J., Jullo, E., et al. 2016, *A&A*, 588, A99
- Lumb, D. H., Warwick, R. S., Page, M., & De Luca, A. 2002, *A&A*, 389, 93
- Mahdavi, A., Hoekstra, H., Babul, A., et al. 2013, *ApJ*, 767, 116
- Mantz, A. B., Allen, S. W., Morris, R. G., et al. 2014, *MNRAS*, 440, 2077
- Markevitch, M. 2010, <http://cxc.cfa.harvard.edu/contrib/maxim/>
- Martino, R., Mazzotta, P., Bourdin, H., et al. 2014, *MNRAS*, 443, 2342

- Mazzotta, P., Rasia, E., Moscardini, L., & Tormen, G. 2004, *MNRAS*, **354**, 10
- Morrison, R., & McCammon, D. 1983, *ApJ*, **270**, 119
- Parmar, A. N., Guainazzi, M., Oosterbroek, T., et al. 1999, *A&A*, **345**, 611
- Pen, U.-L. 1997, *New Astron.*, **2**, 309
- Planck Collaboration XI. 2011, *A&A*, **536**, A11
- Planck Collaboration Int. III. 2013, *A&A*, **550**, A129
- Planck Collaboration XX. 2014, *A&A*, **571**, A20
- Pratt, G. W., Böhringer, H., Croston, J. H., et al. 2007, *A&A*, **461**, 71
- Pratt, G. W., Croston, J. H., Arnaud, M., & Böhringer, H. 2009, *A&A*, **498**, 361
- Sasaki, S. 1996, *PASJ*, **48**, L119
- Schellenberger, G., Reiprich, T. H., Lovisari, L., Nevalainen, J., & David, L. 2015, *A&A*, **575**, A30
- Snowden, S. L., Freyberg, M. J., Plucinsky, P. P., et al. 1995, *ApJ*, **454**, 643
- Snowden, S. L., Mushotzky, R. F., Kuntz, K. D., & Davis, D. S. 2008, *A&A*, **478**, 615
- Starck, J.-L., Murtagh, F., & Bijaoui, A. 1998, *Image Processing and Data Analysis: The Multiscale Approach* (New York: Cambridge University Press)
- Strüder, L., Briel, U., Dennerl, K., et al. 2001, *A&A*, **365**, L18
- Turner, M. J. L., Abbey, A., Arnaud, M., et al. 2001, *A&A*, **365**, L27
- Vikhlinin, A. 2006, *ApJ*, **640**, 710
- Vikhlinin, A., Kravtsov, A., Forman, W., et al. 2006, *ApJ*, **640**, 691
- Vikhlinin, A., Burenin, R. A., Ebeling, H., et al. 2009a, *ApJ*, **692**, 1033
- Vikhlinin, A., Kravtsov, A. V., Burenin, R. A., et al. 2009b, *ApJ*, **692**, 1060
- Voit, G. M. 2005, *Rev. Mod. Phys.*, **77**, 207

Appendix A: *Chandra* and *XMM-Newton* data reduction

A.1. *Chandra* data reduction

Chandra data were cleaned using the *Chandra* Interactive Analysis of Observations (CIAO, [Fruscione et al. 2006](#)) tools version 4.7 and the *Chandra*-ACIS calibration database version 4.6.5 of December 2014. We reprocessed level 1 event files using the `chandra_repro` tool to apply the latest calibration files and produce new bad pixel maps. Events that are likely to be due to high energetic particles were flagged using the GRADE keyword and are removed from the analysis. In addition to the GRADE filtering we also applied the Very Faint mode filtering which further reduces the particle contamination⁴.

To remove periods affected by flare contamination we followed the procedures described in [Hickox & Markevitch \(2006\)](#) and in the *Chandra* background COOKBOOK [Markevitch \(2010\)](#). For ACIS-I observations we extracted the light curve from the four ACIS-I CCDs with a temporal bin of 259.28 s in the [0.3–12] keV band. For ACIS-S observations we extracted the light-curve from CCD S3 with a bin of 1037.12 s in the [2.5–7] keV band. We then computed a mean value by fitting a Poisson distribution on the histogram of the lightcurve, using the `lc_clean` script. We excluded from the analysis all time intervals where the count rate deviates more than 3σ from the mean value.

A.2. *XMM-Newton* data reduction

XMM-Newton datasets were analysed using the Science Analysis System (SAS⁵) version 15.0 and the current calibration files as available to January 2017. Object data files were reprocessed to apply up-to-date calibration files, indexed by the `cifbuild`, using the `emchain` tool. From processed data we removed periods contaminated by flares following the procedures described in [Pratt et al. \(2007\)](#). We extracted the lightcurves from each instrument and we used a Poisson curve to fit the light curve histogram and exclude periods where the count rate exceeds 3σ .

After the flare removal stage we applied a further cleaning filter based on the PATTERN keyword. Similar to the GRADE of *Chandra* this keyword is used to flag photons which are likely to be produced by the interaction of high energetic particles with the detector. Events whose PATTERN keyword is greater than 13 and 4, for the MOS1–2 and PN cameras, respectively, are removed from the analysis. After the cleaning stage, the three camera datasets were combined.

A.3. Point source masking

We identified point sources in *Chandra* datasets running the CIAO wavelet detection tool `wavdetect` ([Freeman et al. 2002](#)) on [0.5–1.2], [1.2–2] and [2–7] keV exposure-corrected images. To detect point sources in *XMM-Newton* datasets we run the Multiresolution wavelet software ([Starck et al. 1998](#)) on the exposure-corrected [0.3–2] keV and [2–5] keV images. Both lists of regions were inspected by eye to check for false positives or missed sources and then merged, in order to remove the same regions from the analysis. In addition to the point sources, we masked the emission coming from the three sub-structures of MACSJ0717.5+3745, two in the south-east sector and one in

the north-west (corresponding to the substructures identified as A, C, and D in [Limousin et al. 2016](#)).

A.4. Background estimation

X-ray observations suffer from background contamination. This background can be divided into two components: instrumental and sky. The first component is due to the interaction of the instrument with high energy particles. Despite the filtering processes there is a residual component which contaminates the observations. The sky component is due to the Galactic emission (e.g. [Snowden et al. 1995](#)) and the CXB due to the superposition of unresolved point-sources (e.g. [Giacconi et al. 2001](#)). When dealing with extended sources which nearly fill the field of view, as for the galaxy clusters, we needed dedicated datasets to estimate and subtract the local background. For *Chandra* and *XMM-Newton* there are two set of datasets. The first one, namely the blank sky dataset, results from the stacking of observations free from diffuse emission where all the point sources have been removed. This dataset represents the average total background (sky plus instrumental). The second set of datasets was formed by specific observations tailored to isolate the instrumental component, that is, to block the light coming from the telescope. For *Chandra* this is achieved by moving the instrument away from the focal plane and the resulting observations are the “stowed” datasets. For *XMM-Newton* “closed” datasets are obtained by observing with a configuration of the filter wheel which blocks the light from the mirrors. In this work we used the latter datasets to remove the instrumental contribution only since this allows us to estimate the sky background component using physically motivated models. That is, using blank sky datasets may result in an overestimate of the local sky background which results in using negative models to account for the over-subtraction⁶.

Instrumental background datasets were cleaned following the same criteria used for observations and skycasted to match the same aimpoint and roll-angle. In particular, *Chandra* stowed datasets are selected to match the same background period as the observation (see [Markevitch 2010](#) for the background period classification). Closed datasets were normalised to the observation in the [10–12], [12–14] keV for MOS1, MOS2 and PN cameras, respectively. Stowed datasets were normalised in the [9.5–10.6] keV band in order to minimise line contamination at high energy ([Bartalucci et al. 2014](#)). The same point source defined for the observation is then applied to the instrumental datasets. The sky component is evaluated differently when dealing with surface brightness or temperature profiles extraction so the subtraction process is described in Sects. 3.2 and in 3.3, respectively.

We also produce datasets accounting for the out of time (OOT) or read out events, which are artefacts related to the presence of very bright sources. We used the method described in [Markevitch \(2010\)](#) and the `epchain` tool to generate the OOT background datasets for *Chandra* and *XMM-Newton*, respectively. These datasets were then processed in the same way as the instrumental background and normalised accordingly. Since the instrumental plus particle and OOT datasets were always summed in our analysis from now on we will refer to the two only as the instrumental background. It is worth noting that the V06/V09 sample was analysed using the *Chandra* blank sky datasets.

⁴ cxc.harvard.edu/cal/Acis/Cal_prods/vfbkggrnd

⁵ cosmos.esa.int/web/xmm-newton

⁶ Another approach is the use of an analytical model for the background (e.g. [Bartalucci et al. 2014](#)).

Table A.1. Minimum and maximum values of the median of the profiles ratio (black solid line) for all the test presented in Sect. 4.

Test name	Section	Figure associated	Min/Max [%]
XMM (PX1) over CXO published in V06/V09	Sect. 4.1	Fig. 1	-3 /+2
Par. CXO n_e over CXO n_e published in V06/V09, normalised at $0.15R_{500}$	Sect. 4.2	Fig. 2	-1 /+5
Dep. CXO n_e over par. CXO n_e	Sect. 4.3	Fig. 3	-2 /+2
Dep. XMM n_e over par. XMM n_e	Sect. 4.3	Fig. 3	-2 /+1
CXO Λ over CXO Λ computed using XMM kT profiles	Sect. 4.4	Fig. 4	-1 /+1
XMM n_e 2D kT over XMM n_e 3D kT in the 0.3–2 keV band	Sect. 4.4	Fig. 5	-0 /+0*
XMM n_e 2D kT over XMM n_e 3D kT in the 2–5 keV band	Sect. 4.4	Fig. 5	-2 /+2
CXO dep. n_e over XMM dep. n_e , normalised at $0.15 R_{500}$	Sect. 4.5.1	Fig. 6	-5 /+2
XMM dep. n_e computed in the (2–5) keV band over the dep. n_e in the (0.3–2) keV band	Sect. 4.5.2	Fig. 7	-2 /+3

Notes. The values are expressed in term of % variation respect to one. (*) The variations are less than 0.5%.

Appendix B: *Chandra* weight evaluation

Analogously to the *XMM-Newton* *evigweight* tool, we wanted to evaluate the effective area for each event in function of its precise position (on the detector) and energy also for the *Chandra* dataset. We used the CIAO *eff2evt* tool to compute the necessary terms which determined the effective area. To avoid confusion with the tool nomenclature, the outputs for each event are the quantum efficiency (QE), the dead area correction (DACORR) and the “effective area” (\widetilde{EA}). This latter term is *not* the same as $EA(i, j, e)$ in Eq. (1). \widetilde{EA} takes into account only effects related to mirrors. The effective area for each event, using this tool, is:

$$EA(i, j, e) = QE(i, j, e) \times DACORR(i, j, e) \times \widetilde{EA}(i, j, e), \quad (\text{B.1})$$

where QE and DACORR are unitless quantities and \widetilde{EA} is in cm^2 .

This tool was conceived to analyse point sources, so we performed several tests to verify that the tool can also be applied to extended source analysis. The first test was to evaluate the impact of using the energy of the photon, which is affected by

instrument degradation problems, to evaluate the effective area. We extracted the RMF for each tile of each ACIS CCD in order to carefully map the energy response. For each photon we then determined the most likely energy and computed the $EA(i, j, \tilde{e})$, where \tilde{e} is the corrected energy, and compare to $EA(i, j, e)$. In the energy range of interest used in this work, [0.7, 10] keV, we do not find significant differences. An additional test is described in Sect. 4.2.

During the observation the *Chandra* telescope was set in a “dithering” motion. The aimpoint insists on different pixels and the resulting effective area changes because of the instrumental effects. For this reason, we can not define the same $EA(i0, j0, e)$ as for *XMM-Newton*. We computed an average value over time using the *mkarf* tool, which evaluates the effective area at a given detector position using the appropriate CALDB files and averages over the observation time.

Appendix C: Test summary

We report in Table A.1 the minimum and maximum values of the median of the ratio computed for each test described in Sect. 4.

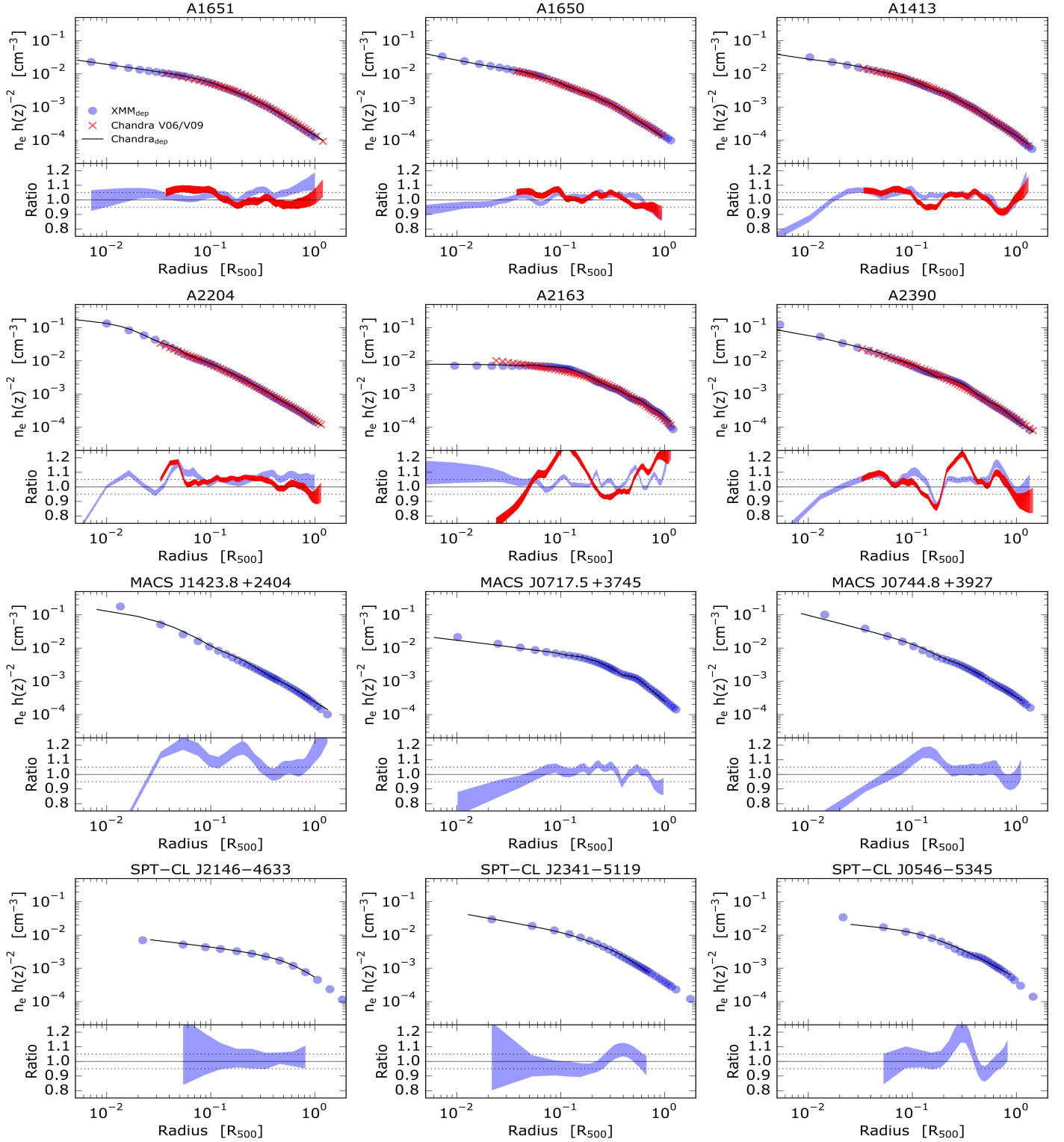


Fig. C.1. For each panel, top: deprojected scaled density profile obtained using *Chandra* and *XMM-Newton* plotted using black solid line and blue points, respectively. We also show the parametric density profiles in V06 with red crosses. For each panel, bottom: ratio between the *Chandra* and the *XMM-Newton* density profiles and between our *Chandra* and V06/V09 samples using blue and red shaded areas, respectively. The solid line and the dotted lines represent the unity and the $\pm 5\%$ levels, respectively.

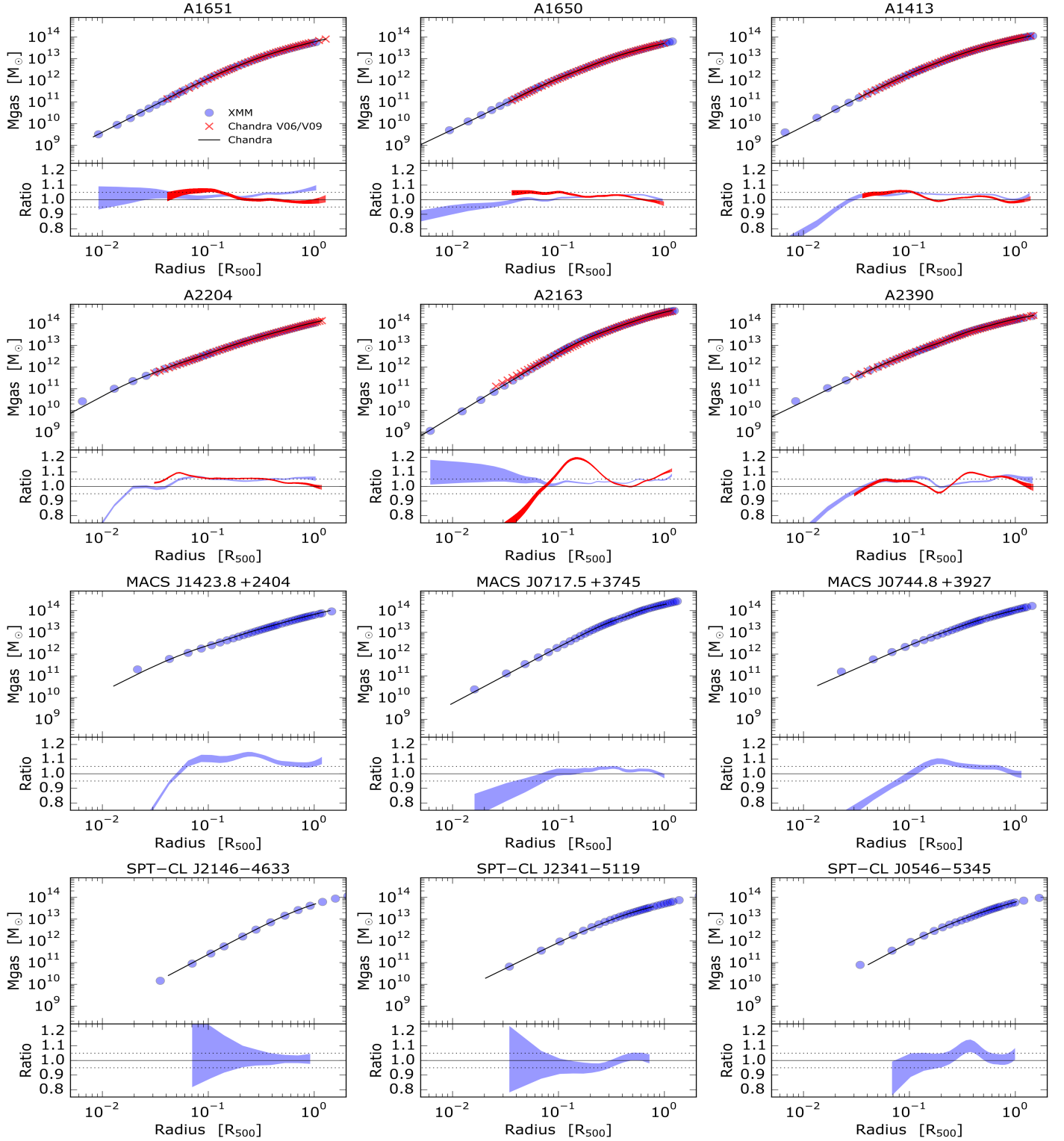


Fig. C.2. Same as Fig. C.1, except that we show the gas mass profiles.